remote sensing

MDPI

Communication

Coseismic Rupture Model and Tectonic Implications of the January 7 2022, Menyuan Mw 6.6 Earthquake Constraints from InSAR Observations and Field Investigation

Yongsheng Li [1], Wenliang Jiang [1], Yujiang Li [1,*], Wenhao Shen [1], Zhongtai He [1], Bingquan Li [2], Qiang Li [1], Qisong Jiao [1] and Yunfeng Tian [1]

[1] National Institute of Natural Hazards, Ministry of Emergency Management of China, Beijing 100085, China; yongshengli@ninhm.ac.cn (Y.L.); jiang_wenliang@163.com (W.J.); shenxiaoxi200212@163.com (W.S.); zhongtaihe@ninhm.ac.cn (Z.H.); liqiang08@163.com (Q.L.); 1985jqs@163.com (Q.J.); y.f.tian@163.com (Y.T.)
[2] School of Automation, China University of Geoscience, Wuhan 430074, China; bingquanli@cug.edu.cn
* Correspondence: yujiangli@ninhm.ac.cn

Abstract: A Mw 6.6 earthquake struck Menyuan, Qinghai, China, on 7 January 2022. To determine the rupture parameters of this event, the coseismic InSAR deformation fields were mapped and further employed to estimate the focal mechanism. The best-fitting solution emphasized that the 2022 Menyuan earthquake ruptured at the junction of the Tuolaishan fault and the Lenglongling fault. Both rupturing faults were dominated by sinistral strike-slip, and the main slip was concentrated on the shallow part of the rupture plane. The latter was the main rupture segment with a strike of 106° and a dip of 86°. The slip mainly occurred at depths of 0–8 km, and the rupture was exposed at the surface. The maximum slip reached ~3.5 m, which occurred mainly at a depth of 4 km. Joint analysis of the optimal slip model, relocated aftershocks, Coulomb stress change, and field observation suggested that the strain energy in the Tuolaishan fault may not have been fully released and needs further attention. Moreover, the 2022 Mw6.6 Menyuan earthquake caused a significant stress loading effect on the western Tuolaishan fault and eastern Lenglongling fault, which implies that the 2022 event increased the seismic hazard in these regions.

Keywords: 2022 Menyuan earthquake; Lenglongling fault; InSAR; NE Qinghai-Tibetan Plateau; seismic hazard

check for updates

Citation: Li, Y.; Jiang, W.; Li, Y.; Shen, W.; He, Z.; Li, B.; Li, Q.; Jiao, Q.; Tian, Y. Coseismic Rupture Model and Tectonic Implications of the January 7 2022, Menyuan Mw 6.6 Earthquake Constraints from InSAR Observations and Field Investigation. *Remote Sens.* **2022**, *14*, 2111. https://doi.org/10.3390/rs14092111

Academic Editor: Salvatore Stramondo

Received: 18 March 2022
Accepted: 26 April 2022
Published: 28 April 2022

1. Introduction

On 7 January 2022, a Mw 6.6 earthquake occurred in Menyuan, Qinghai, China (37.77°N, 101.26°E), and the depth of the hypocenter was 10 km. The epicenter was located in the high mountainous area on the southern border of the Qilian Mountains on the northeastern Qinghai-Tibetan Plateau (QTP) (Figure 1). The average elevation within 5 km of the epicenter is approximately 3600 m above sea level. The earthquake occurred on the Lenglongling strike-slip fault, extending westward from the Haiyuan-Laohushan fault zone to the Qilian Mountain area [1–3]. The fault undergoes mainly sinistral strike-slip with a small reverse component [4,5]. Near the epicenter, the Lenglongling fault (LLLF) has several branch faults, and the strike of the main fault deflects to the west to form a tensile bend. It is a section that easily accumulates elastic strain energy and releases energy to produce moderately strong earthquakes [6–9]. After an earthquake, exploring slip models and rupture parameters of the fault is critical to investigate the geological structures better and assess potential earthquake hazard models. Many solutions for the focal mechanisms of this earthquake have been obtained using different methods and data sources (Table S1). These focal mechanisms have various degrees of uncertainty, which causes difficulties in seismic dynamic analysis and other applications. The rapid products of the focal mechanism for most earthquakes are inverted from the seismic-wave

data. Generally, these products employ a single fault model for fast inversion. For some moderate–strong earthquakes, complicated multi-fault models are necessary.

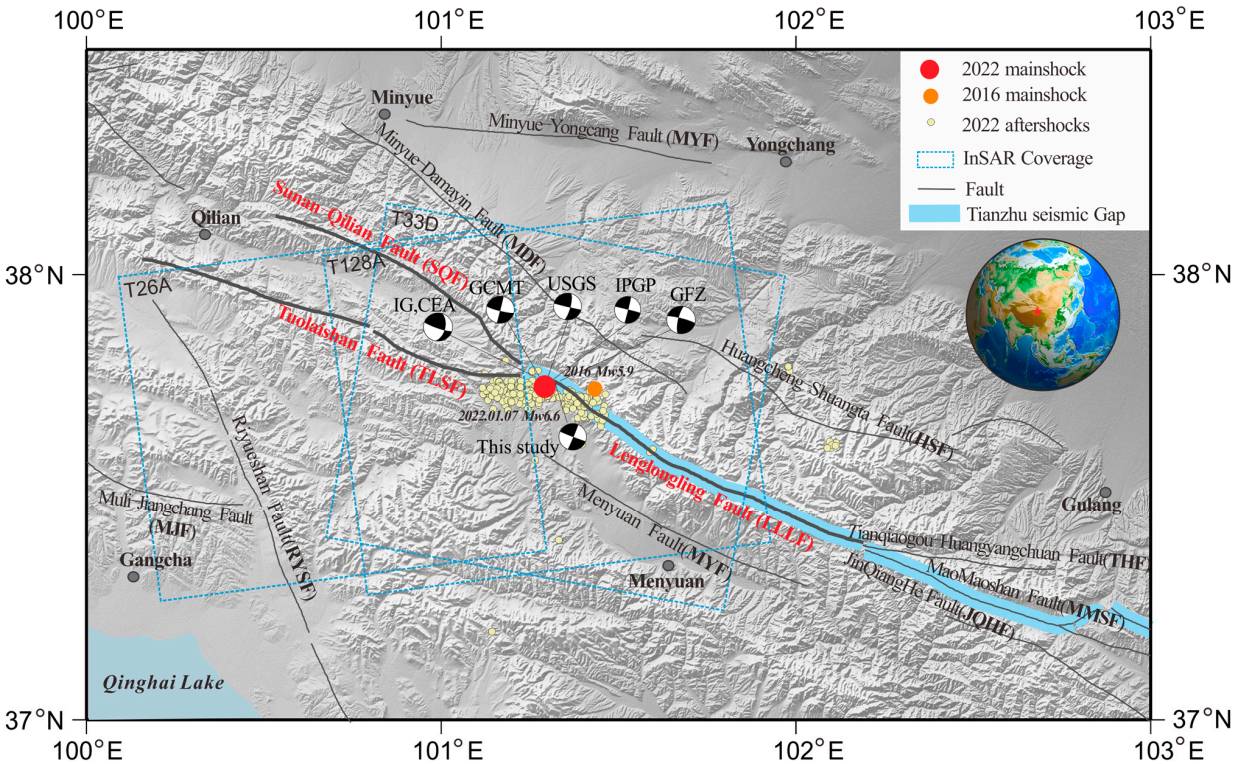

Figure 1. Active faults and seismotectonic background of the region surrounding the 2022 Menyuan earthquake. The red dot represents the 2022 Menyuan earthquake, and the faults are referred from [6,10,11]. The yellow points indicate the aftershocks [12].

In this paper, both descending and ascending track data from Sentinel-1 are employed to obtain the coseismic deformation fields of the 2022 Menyuan earthquake (Figure 1). Then, a further inversion is applied to estimate the key parameters, such as the rupture geometry and slip distribution characteristics. With the constraints from the field investigation, the seismic rupture zone and stress release are analyzed in detail. The 2016 and 2022 earthquake events present chances to explore the formation mechanism better and seismotectonic of the LLLF zone and nearby regions, which have great significance in assessing the recent trend of strong earthquake activity on the NE QTP.

2. Tectonic Setting

The formation and development of the QTP are driven by a continuous collision between the Indian and Eurasian Plates. The oblique movement between the Indian Plate and the Eurasian Plates causes interactions at the edge of the plateau, leading to earthquake-prone faults. A Mw 7.3 earthquake occurred on 21 May 2021 in Madou. The 2021 earthquake was 500 km away from the 2022 Menyuan quake event; it was too far to influence the event in LLLF directly. The LLLF zone is an intraplate region located on the northern margin of the QTP and exhibits left-lateral and oblique-slip along its western segment during the Quaternary [1] (Figure 1). The LLLF is developed along the watershed of the Qilian Mountains, with a strike of 110–115° and an overall length of more than 120 km [4]. This fault zone is connected to the Huangyangchuan fault and the Jinqianghe fault to the east. The western end is connected to the Qilian-Sunan fault zone and Tuolaishan fault (TLSF) (Figure 1). Current research suggests that the fault has been very active during the Holocene, forming many large-scale faulted landforms at the surface, such as gullies, terraces, ridges, and moraines distributed along the fault zone, and some synchronous left-lateral faults are distributed in many typical areas [1–3].

The GPS velocity fields and strain rates [13,14] suggest that the structural deformation on the northeastern margin of the QTP rotates clockwise due to the obstruction of the Ordos and Gobi-Alashan blocks. The direction gradually changes from NE thrusting in the west to sinistral strike-slip along the Qilian-Haiyuan structural belt, and the strain direction changes from ESE to SSE [4] (Figure 2). Along the Qilian-Haiyuan structural belt, the deformation gradually transitions to sinistral strike-slip, especially in the LLLF zone. According to the Holocene fault landform analysis, the displacement of a single earthquake event in the western section of the LLLF zone is significantly lower than that in the eastern section. In the westernmost section of the Qilian-Haiyuan structural belt, the near-parallel TLSF zone and Qilian-Sunan fault zone mainly regulate regional tectonic deformation by obvious thrusting [9]. The cumulative displacement along the fault zone increases significantly from west to east, indicating that the western section of the LLLF zone is dominated by compressive and shear tension (e.g., 2016 Menyuan earthquake) [7], while the eastern segment of the LLLF zone exhibits sinistral strike-slip movement, which suggests that the LLLF zone plays an important role in adjusting the tectonic deformation in the NE QTP.

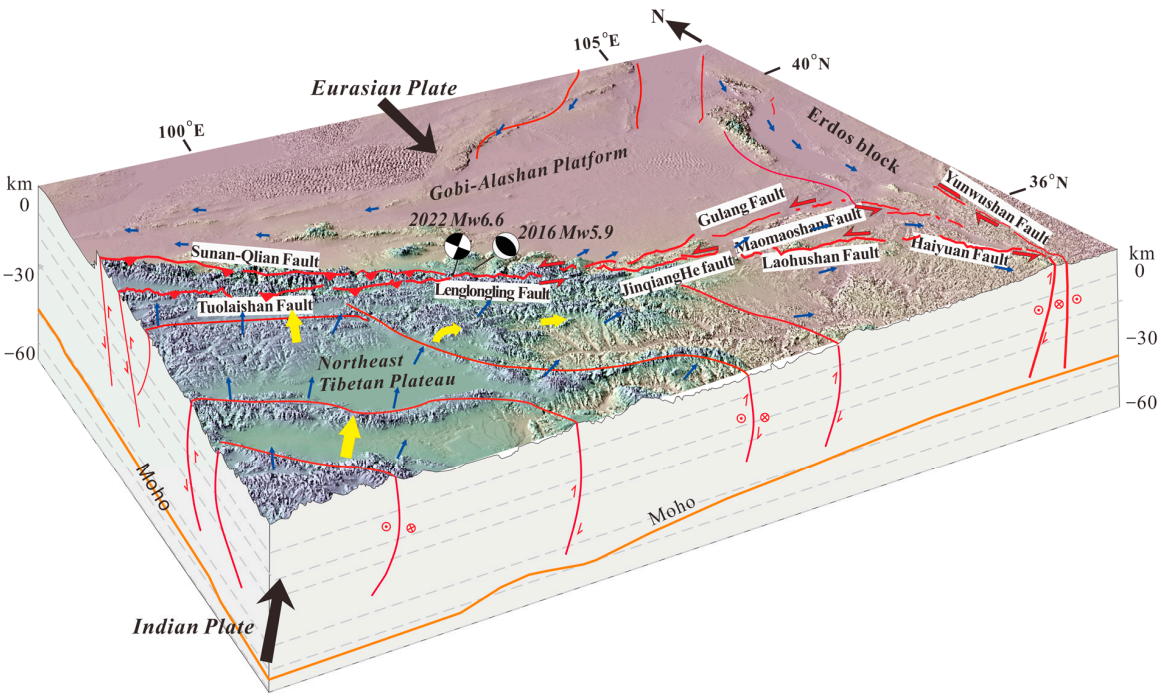

Figure 2. Comprehensive seismotectonic model of the LLLF zone and surrounding areas. The thick yellow arrows indicate the directions of plate movements. The narrow blue arrows indicate the GPS velocity field with the Gobi-Alashan block referenced from [13]. Profiles of the Haiyuan and Yunwushan fault zones are referenced from [15]. Profiles of the Tuolaishan and Qilian-Sunan fault zones are referenced from [16,17]. The Moho depth is referenced from [18,19].

The 2022 Menyuan earthquake occurred on an east-west trending sinistral fault within the Qilian-Haiyuan tectonic belt. It comprises several active sinistral strike-slip fault zones with WNW-ESE strikes and oblique en echelon arrangements. These fault zones play a crucial role in regulating and transforming the tectonic deformation in the northeastern QTP [4,5,9]. The focal mechanism of this earthquake was similar to those of other earthquake events that occurred in or near the Haiyuan fault system [6]. This event occurred in the strike-slip compression zone corresponding to the bend in the LLLF zone. By 17 January 2022, more than 500 aftershocks had occurred (Figure 1), and the maximum aftershock moment magnitude was M 5.3 [12]. These aftershocks were mainly located along approximately 40 km of the rupturing fault. The aftershocks distributed on the western end of the rupture reflected a nearly east-west trending fault and were consistent

with the nearly east-west strike of the TLSF. In contrast, the aftershocks on the eastern side of the rupture were mainly distributed along the LLLF. Thus, both the LLLF and TLSF may have contributed to this earthquake event. No Mw > 7.0 earthquake has ever been recorded in the LLLF zone. However, two Mw 5.9 earthquakes occurred in the LLLF zone on 26 August 1986 and 21 January 2016 [7]. The present-day tectonic slip rate is approximately 6.6 ± 0.3 mm/year [4,14]. Whether the two earthquakes in 2016 and 2022 resolved the Tianzhu seismic gap and whether a larger earthquake will occur should receive more attention [1].

3. InSAR Coseismic Deformation

3.1. InSAR Data and Methodology

To characterize the coseismic deformation fields of the 2022 Menyuan earthquake event, this paper adopted three Sentinel-1A pairs (T26, T33, and T128) with ascending and descending tracks (Figure 1 and Table S2). The Sentinel-1 SAR-Based Coseismic Deformation Monitoring Service was triggered by USGS earthquake hazard alert systems, and the SAR data were automatically searched, downloaded, and processed. Then, the coseismic deformation fields were obtained [20]. ALOS World 3D with a 30 m resolution was employed as external digital elevation model (DEM) data to eliminate the phase contribution of terrain turbulence [21]. Multilook processing with a factor of 10:2 was adopted in interferometric processing to suppress the noise and improve the signal-to-noise ratio (SNR). The minimum cost flow (MCF) method was employed to unwrap the phase [22]. The external atmospheric delay product from Generic Atmospheric Correction Online Service for InSAR (GACOS) [23,24] was employed to reduce the tropospheric delay errors and terrain-correlated atmospheric phase delay (TCAD) (Figure S1). To reduce the orbital residual derived from the possible inaccurate ephemeris parameters, we estimated a polynomial function with the observation data in the far-field nondeformed region to remove the estimated phase ramp [25] (Figure S2). The results show that the atmospheric delay error and orbital residual components in the interferogram were much smaller than the coseismic deformation signal and can be ignored. After eliminating the possible error contribution, the final coseismic deformation fields were obtained (Figure 3).

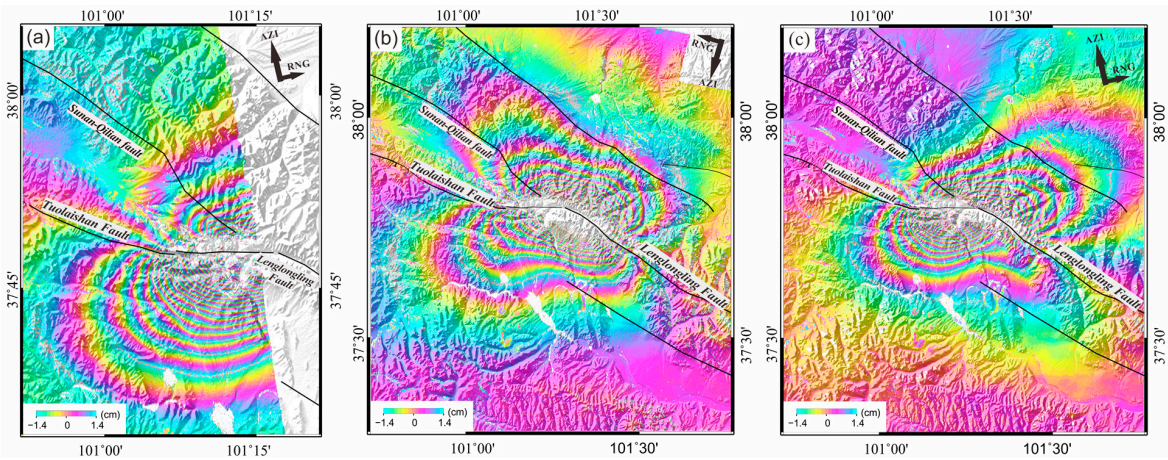

Figure 3. (**a**) Coseismic deformation of the 2022 Menyuan earthquake event derived from Sentinel-1 Ascending Track 26. (**b**) Coseismic deformation fields from Descending Track 33. (**c**) Coseismic deformation fields from Ascending Track 128. The black lines indicate faults distributed near the epicenter.

3.2. Coseismic Deformation

The sinistral strike-slip trend of the LLLF is nearly east-west. In addition, the epicenter is located on the northwestern edge of the QTP, with a dry climate and sparse vegetation, so it shows very high coherence on the interferograms (Figure 3). The coseismic deformation fields of the three tracks illustrate that this earthquake produced a conspicuous butterfly-shaped pattern and revealed complex surface deformation characteristics (Figure 3b,c).

From the results of different track data, the two walls show opposite deformation trends, which is consistent with the concept that this earthquake was a rupture event dominated by sinistral strike-slip faults. Moreover, we note a loss of coherence in the meizoseismal region. The reason for this phenomenon is that the thick snow cover reduced the coherence of the interferogram. In addition, the rupture deformation gradient near the epicenter exceeded the deformation measurement capability of the Sentinel-1 satellite, resulting in the discontinuity of the deformation phase. Nevertheless, the interferograms describe the overall deformation characteristics of the earthquake well. The results from Descending Track 33 confirmed that the maximum line-of-sight (LOS) deformations are approximately 70 cm and 80 cm, respectively, on the northern and southern sides of the inferred faults (Figure 3b), while they are approximately 40 cm and 60 cm, respectively, along ascending path 128 (Figure 3c). These deformations are mainly concentrated at the junction of the LLLF and TLSF, which implies that the eastern section of the TLSF and the western section of the LLLF ruptured simultaneously.

4. Focal Mechanism Inversion

4.1. Determination of the Surface Rupture Fault

According to the field investigation, this earthquake caused many significant surface ruptures. The interpreted results from Gaofen-7 satellite images indicate that the surface rupture length is more than 20 km [26]. This paper employs the pixel offset tracking (POT) method [27] and Sentinel-1 Descending Track 33 images to explore the surface rupture zone. The long-wavelength distortions by orbital/ionospheric error will usually bring an error term in pixel offset tracing. We employed a similar plane fitting method in Section 3.1 and conducted an orbital error correction to reduce the orbital residual components of the POT in the range direction (Figure S3). Compared to coseismic deformation signals, the errors of orbit and ionosphere in the original POT results are relatively small, indicating that the orbit-related long-wavelength error in the original POT result can be ignored. The POT results provide an essential constraint for the inversion of this earthquake, especially their strike parameters (Figure 4). The results show that azimuth deformation is not apparent (Figure 4a). In contrast, the deformation in the range direction is intense (Figure 4b), which also validates the characteristics of the E-W strike-slip. According to the interpretation of the POT results, the western segment of the inferred rupture coincides with the LLLF zone, while the eastern segment overlaps with the TLSF. Therefore, the rupture process of this earthquake resulted from the joint action of the two faults.

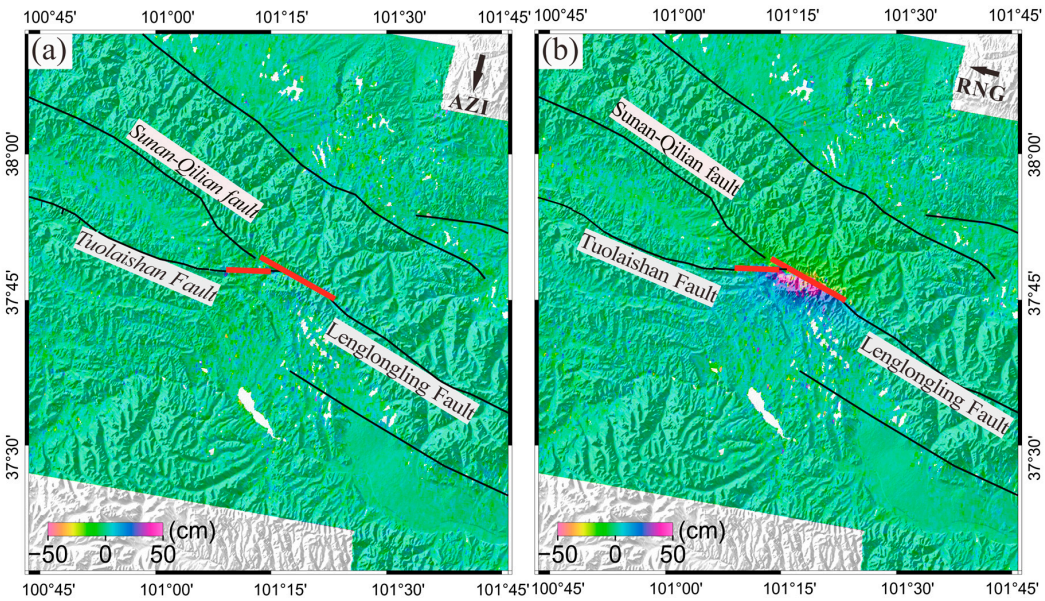

Figure 4. Rupture faults are determined by pixel offset tracking. (**a**) deformation in the azimuth direction and (**b**) deformation in the range direction. The red lines indicate inferred rupture faults.

4.2. Uniform Slip Model

Since Ascending Track 128 and Descending Track 33 can completely cover the whole deformation field of this earthquake event (Figure 3b,c), we selected them as the observation constraints for further inversion processes. The elastic half-space rectangular dislocation theory was applied to the inverse uniform slip of this earthquake [28]. By comprehensively considering the overall distribution of the aftershock sequence (Figure 1), the characteristics of the coseismic deformation interferogram (Figure 3b,c), and the focal mechanism solutions resolved by other sources (Table S1), we constructed a uniform slip model with two nearly east-west trending sinistral strike-slip planes. A rupture model with two hypothetical faults was determined to be responsible for this earthquake. They represented the LLLF and TLSF (Figure 4b), and we assumed that the strikes of the faults ranged from 105° to 120° and from 80° to 100°, respectively. These faults are high dipping sinistral strike-slip faults, so we set dip angles ranging from 80° to 89° and slip angles ranging from −20° to 20°. The particle swarm optimization method was adopted to seek the optimal location, strike, dip angle, slip angle, fault width, length, burial depth of the upper boundary of the fault, and slip amount [29]. The Gaussian errors were added to the original observations to evaluate the uncertainties in the nonlinear inversion. Then, we estimated the trade-offs for the geometric parameters by a Monte Carlo analysis with 100 perturbed datasets, and the minor uncertainties implied that the nonlinear inversion has high reliability (Figure S4). The optimal results emphasized that this earthquake ruptured on two faults, one is a nearly east-west trending sinistral strike-slip fault with a length of ~20 km, which has a minor reverse fault component (rake angle is ~−5° and strike angle of ~106°), and the other is a 10 km pure east-west sinistral strike-slip fault (strike angle of ~89°).

4.3. Distributed Slip Model

Then, we fixed the location and strike angle of the rupture plane derived from the previous optimal rupture parameters, and the lengths and widths of the fault planes were expanded along the strike and dip, respectively. The two fault planes were discretized into a small rectangular grid of 1 km × 1 km. The dip angle was further optimized in the subsequent linear inversion. We applied a logarithmic function to re-estimate the best-fitting dip angle [29]. The optimal slip models revealed that two strike-slip faults dominated the rupturing planes. The western section of the LLLF and the eastern section of the TLSF participated in the rupture simultaneously. The best-fitting solution suggested that the main rupture plane along the LLLF had a strike of ~106°, a dip of ~86°, and a rake of ~−5° and was a strike-slip fault, while the secondary rupture plane along the TLSF had values of ~89°, ~83°, and ~−1°, respectively. The fault slip was mainly distributed in the western segment of the LLLF (Figure 5). The main slip occurred on the shallow part of the rupture plane at depths of 0–8 km, and the maximum slip of 3.5 m was concentrated at a depth of 4 km (Figure 6). The apparent slip could be observed on the shallow rupture plane (0–1 km), implying that the coseismic slip ruptured at the surface (Figure 6). The slip distribution model produced a seismic moment of ~1.0244×10^{19} Nm, equivalent to an earthquake with Mw 6.6 and consistent with the results from other sources (Table S1). Figure 5 indicates that the mainshock triggered abundant aftershocks at depths of 7–14 km, mainly concentrated below the main rupture region of this earthquake. To validate the inversion reliability of the approach, we estimated the surface deformation derived from the optimal distributed slip model and both tracks of SAR geometry. The simulated interferograms (Figure 7b,e) accurately fit the observation deformation of both tracks and can better explain the spatial distribution of the coseismic deformation field. The residuals are small (Figure 7c,f), which implies that the rupture model estimated in this paper has high reliability.

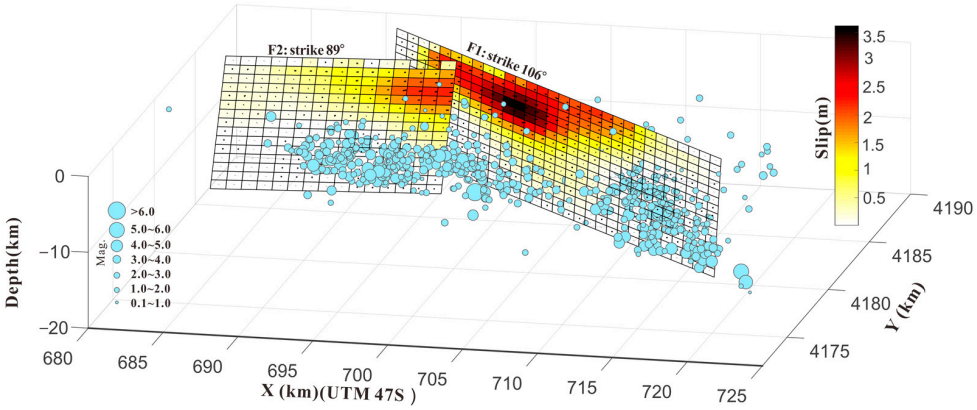

Figure 5. The slip model of the rupture faults of the 2022 Menyuan earthquake. The blue points represent the mainshock and 584 aftershocks through 17 January 2022 (1 with M $\geq$ 5, 5 with 4.0 $\leq$ M $\leq$ 4.9, 19 with 3.0 $\leq$ M $\leq$ 3.9, and 559 with M < 3).

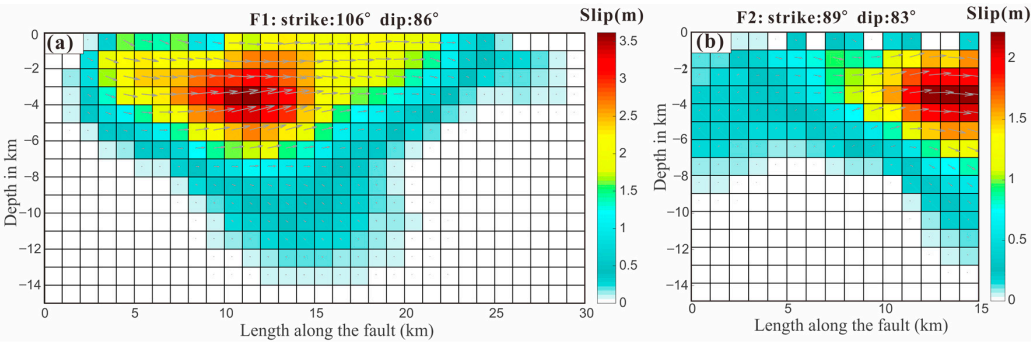

Figure 6. Optimal slip distributions of the 2022 earthquake event.

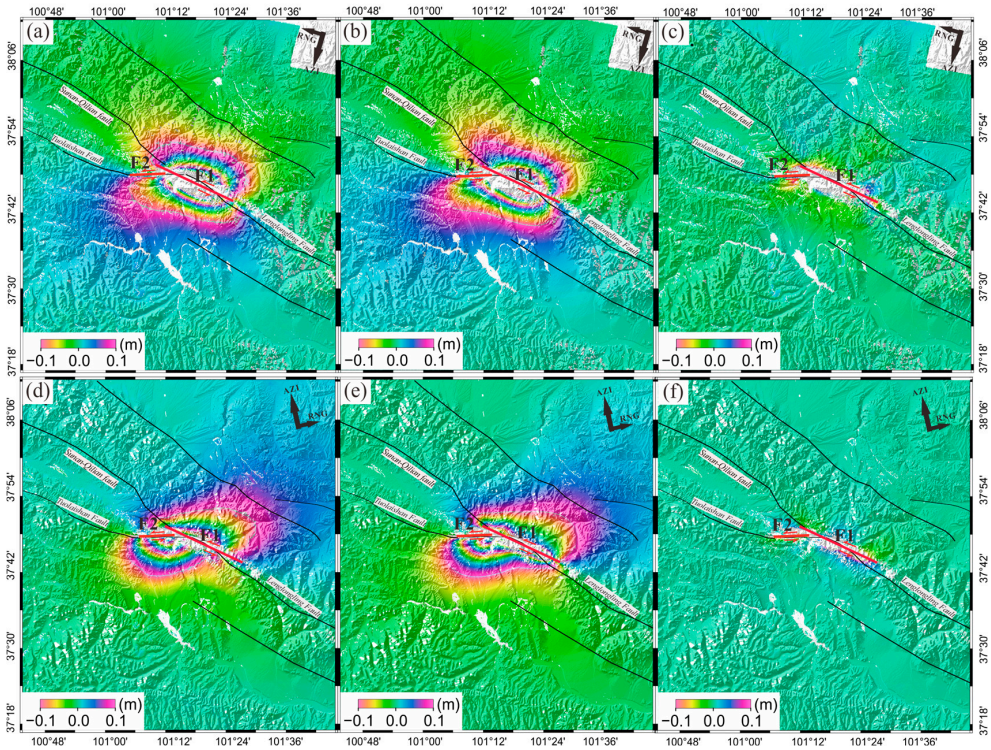

Figure 7. Coseismic deformation fields of the 2022 Menyuan earthquake. (**a**,**d**) show the observed coseismic deformation for Descending Track 33 and Ascending Track 128, respectively. (**b**,**e**) represent simulated deformation maps. (**c**,**f**) represent the residuals. F1: rupturing segment of the LLLF, F2: rupturing segment of the TLSF.

4.4. Coulomb Stress Changes

The Coulomb stress change (ΔCFS) caused by the 2022 Menyuan earthquake is calculated by Equation (1). A positive ΔCFS promotes the occurrence of subsequent earthquakes [30].

$$\Delta CFS = \Delta\tau + \mu'\Delta\sigma_n \quad (1)$$

where $\Delta\tau$ is the shear stress change on the fault plane, which is positive in the fault slip direction; $\Delta\sigma_n$ is the normal stress change on the fault plane, which is positive for fault unclamping; and μ' is the effective friction coefficient. The coseismic ΔCFS was calculated by applying the elastic dislocation model [28]. A Burgers body was employed to simulate the viscoelastic rheological properties of the lower crust and the upper mantle [31,32]. We adopted the PSGRN/PSCMP code based on a stratified viscoelastic model [33] to calculate the stress changes and analyze the joint effects of the coseismic dislocations and postseismic viscoelastic relaxation. Based on the lithosphere velocity structure and rheological properties around the NE QTP [34–36], we determined the parameters in the viscoelastic stratified model, as shown in Table S3.

We calculated the coseismic ΔCFS associated with the 2022 Mw 6.6 Menyuan earthquake by projecting the stress tensors to the focal parameters of the mainshock. The effective friction coefficient was set as 0.4. Figure 8 shows the projection results of static ΔCFS at depths of 5 km and 10 km on the optimal rupture surface caused by the 2022 Menyuan Mw 6.6 earthquake. We find that the occurrence of the mainshock led to significant changes in ΔCFS on unruptured parts of the LLLF, the TLSF, and some parts of the Minle-Damaying fault (Figure 8). Thus, this event has increased the seismic hazard of these faults along the Tianzhu seismic gap, but the significant stress has decreased on most sections of the Minle-Damaying fault, the Huangcheng fault, the Menyuan fault, and the eastern segment of the Sunan-Qilian fault.

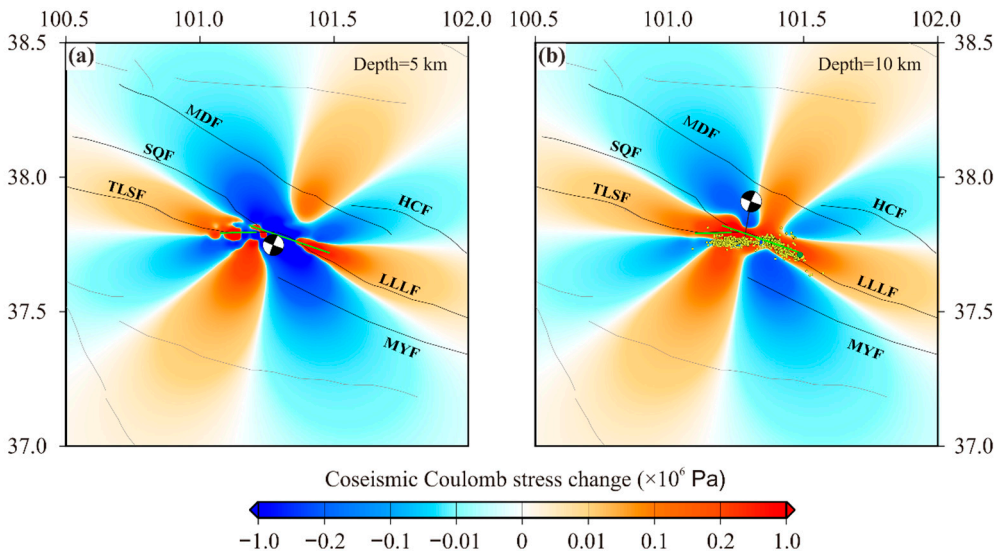

Figure 8. Coseismic ΔCFS was associated with the 2022 Menyuan Mw 6.6 earthquake at depths of 5 km and 10 km. (**a**) represents a depth of 5 km and (**b**) represents 10 km. The black lines indicate the active faults. The green lines represent the rupturing fault inferred from modeling. Yellow points indicate the relocated aftershocks, and the green dot indicates the largest M 5.3 aftershock.

5. Discussion

5.1. Possible Triggering Effect between the 2016 and 2022 Events

After a strong earthquake, the stress state in the seismogenic area is affected, promoting or delaying the occurrence of subsequent earthquakes on active faults in adjacent areas [37,38]. Near the source region of the 2022 Menyuan Mw 6.6 earthquake, the Mw 5.9 Menyuan earthquake occurred in 2016. Considering that the distance between them was approximately 30 km, we further analyzed the possible triggering effect between

these two events. With the coseismic slip model of the 2016 event as the source rupture model [7], we calculated the coseismic and postseismic stress changes associated with the 2016 earthquake by projecting the stress tensors to the focal parameters of the 2022 Mw 6.6 mainshock. The results show that the coseismic normal and shear stress changes at the hypocenter of the 2022 earthquake are -0.16×10^4 Pa and 0.25×10^4 Pa, respectively (Figure 9a,b), indicating the coseismic compressive effect on the rupture plane. According to Equation 1, we find that the 2016 Menyuan earthquake transmitted a positive Coulomb stress change to the 2022 earthquake. In particular, the coseismic Coulomb stress change reaches 0.185×10^4 Pa (Figure 9c), suggesting that the 2016 Menyuan earthquake facilitated the occurrence of the 2022 earthquake, which is consistent with the concept expressed by [27]. Moreover, the postseismic Coulomb stress change is positive, but the impact is limited (Figure 9d). Thus, we conclude that the 2016 Menyuan earthquake promoted the occurrence of the 2022 earthquake.

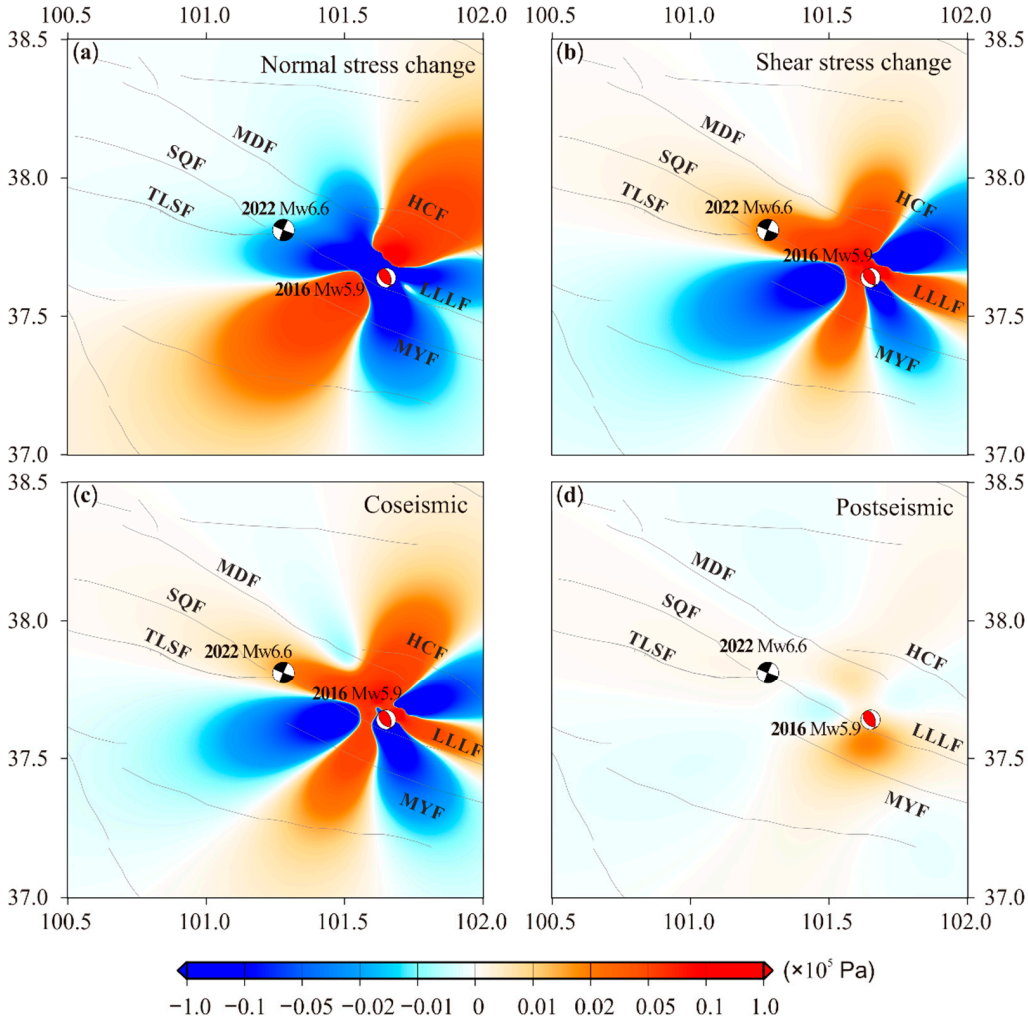

Figure 9. Stress change associated with the 2016 Menyuan earthquake. (**a**) Coseismic normal stress change. (**b**) Coseismic shear stress change. (**c**) Coseismic Coulomb stress change. (**d**) Postseismic Coulomb stress change.

5.2. Was the Coulomb Stress Completely Released by the 2022 Event at Any Depth?

Based on the previous optimal slip model (Figure 6), the ΔCFS caused by the mainshock of the 2022 event was calculated (Figure 8). The statistical results show that 95% of the aftershocks were distributed where Coulomb stress increased (depth = 10 km). In particular, as the remarkable slip was mainly concentrated at 3–5 km (Figure 6), the seismogenic fault may have fully released the accumulated strain energy, as indicated by the significant

decrease in coseismic ΔCFS at a depth of 5 km near the hypocenter (Figure 8a). However, at 10 km depth, because the seismogenic fault released only part of the strain energy, almost the entire source region still expresses the significant increase in coseismic stress change (Figure 8b). This significant stress increase explains well the occurrence of clustered aftershocks that are mainly concentrated at depths of 8–13 km (Figure 5). Furthermore, the largest Mw5.3 aftershock occurred in the region with a high coseismic stress change of 0.33×10^6 Pa, which exceeds the threshold of Coulomb stress triggering, suggesting a triggering effect between the two events.

5.3. The Seismic Hazard on the TLSF Derived from Spatial Diversity of the Surface Rupture

Due to the influence of decorrelation, InSAR technology cannot accurately obtain the deformation pattern in the vicinity of faults of this earthquake (Figure 3). We conducted a field investigation to clarify the surface deformation and the spatial diversity of the surface rupture zone. The field investigation results showed that this earthquake produced two main surface rupture zones (Figure 10). The green dashed lines in Figure 10 represent the surface rupture traces identified in the field investigation, which are consistent with the inferred traces derived from InSAR measurements (red lines in Figure 10). According to the field observations, we selected small gullies, roads, and riverbanks as identification targets and distinguished the surface rupture magnitude by measuring the surface dislocations. We selected six sites along the Lenglongling rupture fault to demonstrate the rupture scale (a–f in Figure 10). We found that the maximum surface rupture was larger than ~270 cm at point f, suggesting that the LLLF rupture was strong. In comparison, the rupture along the TLSF zone was relatively small (g and h in Figure 10). The maximum surface dislocation was ~15−20 cm. Combining this information with the evidence that the main earthquake was initiated in the LLLF zone, we infer that the surface rupture in the eastern section of the TLSF zone was passively induced by the rupturing of the LLLF zone. The distribution and intensity of surface rupture along the TLSF are relatively limited. Comparing Figures 8 and 10 show that this earthquake had a direct stress loading effect on the TLSF. The spatial diversity of the surface rupture zone suggested that the seismic hazard in the TLSF was not reduced due to the occurrence of the 2022 earthquake and should receive continuous attention.

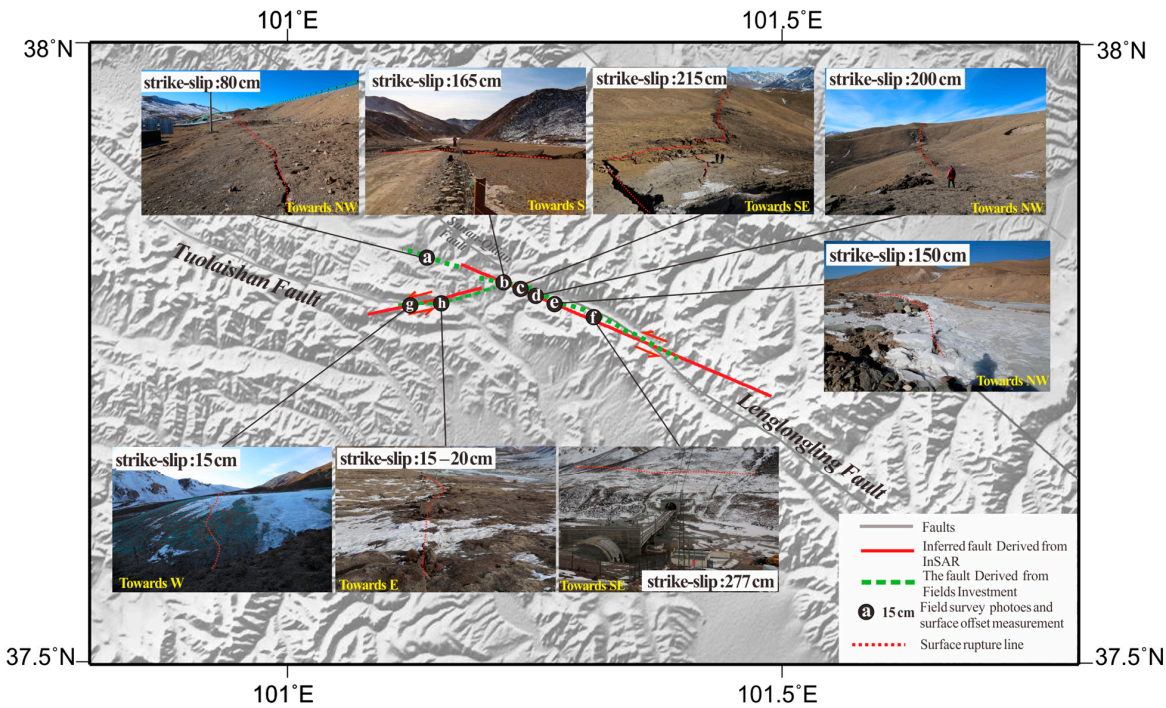

Figure 10. Surface rupture distribution derived from field measurements. Sites a–h are the selected locations for field measurements of surface ruptures.

6. Conclusions

The coseismic deformation maps of the Mw 6.6 Menyuan earthquake on 7 January 2022 were derived from Sentinel-1 ascending and descending tracks. The deformation patterns demonstrated that this earthquake was dominated by a sinistral strike-slip rupturing event and revealed the complex characteristics of coseismic deformation, distributed at the junction of the western section of the LLLF and the eastern section of the TLSF. The geometric structure and optimal slip distribution of the rupture planes were obtained by employing a two-step inversion strategy. The best-fitting solution suggested that both rupturing faults were dominated by sinistral strike-slip. The main slips were concentrated on the shallow parts of the rupture planes. A combined analysis of the optimal slip distribution of the 2022 event and the relocated aftershocks suggested that rare aftershocks occurred in shallow layers (<5 km), while in the deep part (10 km), strain energy may not have been fully released, resulting in abundant aftershocks. Joint analysis of the coseismic and postseismic ΔCFS of the 2016 event led us to conclude that the 2016 earthquake facilitated the occurrence of the 2022 Menyuan earthquake. Combining this result with an analysis of the field investigation, we considered that the strain energy of the TLSF might not have been completely released and that its seismic hazard needs further attention. Clarifying the rupture parameters and tectonic implications of the Menyuan earthquakes is helpful to study further the geological structure and kinematic mechanism of the LLLF and the earthquake risk in the Tianzhu seismic gap.

Supplementary Materials: The following supporting information can be downloaded at: https://www.mdpi.com/article/10.3390/rs14092111/s1, Supplementary Material Figure S1: Correction for the tropospheric delay errors and terrain-correlated atmospheric phase delay (TCAD), the external atmospheric delay product from Generic Atmospheric Correction Online Service for InSAR (GACOS); Supplementary Material Figure S2: The orbit errors correction for descending track 33 and ascending tracking 128; Supplementary Material Figure S3: The long wavelength phase errors correction for the pixel offset tracking in range direction; Supplementary Material Figure S4: Uncertainties and trade-offs for the nonlinear inversion computed using Monte Carlo analysis; Supplementary Material Table S1: Focal mechanisms and rupture parameters from different studies; Supplementary Material Table S2: SAR images used in the InSAR analysis; Supplementary Material Table S3: Parameters in the stratified viscoelastic Burgers model.

Author Contributions: Conceptualization, Y.L. (Yongsheng Li) and Y.L. (Yujiang Li); methodology, W.J., Y.L. (Yongsheng Li) and Y.L. (Yujiang Li); software, Y.L. (Yujiang Li), Y.L. (Yongsheng Li) and W.S.; validation, Z.H.; formal analysis, Q.L., Q.J., Y.T., B.L. and Y.L. (Yongsheng Li); investigation, Z.H., Q.L., Q.J., Y.T. data curation, W.J.; writing—original draft preparation, Y.L. (Yujiang Li); writing—review and editing, Y.L. (Yujiang Li) and Y.L. (Yongsheng Li); visualization, (Yongsheng Li); supervision, Y.L. (Yujiang Li) and Y.L. (Yongsheng Li); funding acquisition, W.J., Y.L. (Yujiang Li) and Y.L. (Yongsheng Li). All authors have read and agreed to the published version of the manuscript.

Funding: This research is partly supported by research grants from the National Institute of Natural Hazards, MEMC (Grant No. ZDJ 2019-17); the National Key Research and Development Program of China (2021YFC3001903); the Gaofen earthquake monitoring and emergency application demonstration (Phase II) (31_Y30F09-9001-20/22) and the National Natural Science Foundation of China (Nos. 41704051, 41874116, and 41772219).

Data Availability Statement: The Sentinel-1 data used in this study are downloaded from the European Space Agency (ESA) through the ASF Data Hub website https://vertex.daac.asf.alaska.edu/ (accessed on 20 January 2022). The PSGRN/PSCMP program is available through the website ftp://ftp.gfz-potsdam.de/home/turk/wang/psgrn+pscmp-2020-code+input.rar (accessed on 20 January 2022).

Acknowledgments: The authors would like to thank Rongjiang Wang for providing the PSGRN/PSCMP software package, Wanpeng Feng for his PSOKINV software and constructive comments, and Fang Lihua for the relocated aftershocks. Most figures were plotted using the Generic Mapping Tools.

Conflicts of Interest: The authors declare no conflict of interest.

References

1. Gaudemer, Y.; Tapponnier, P.; Meyer, B.; Peltzer, G.; Shunmin, G.; Zhitai, C. Partitioning of crustal slip between linked, active faults in the eastern Qilian Shan, and evidence for amajor seismic gap, the Tianzhu gap, on the western Haiyuan fault, Gansu (China). *Geophys. J. R. Astron. Soc.* **1995**, *120*, 599–645. [CrossRef]
2. He, W.; Liu, B.; Yuan, D.; Yang, M. Research on slip rates of the lenglongling active fault zone. *China Earthq. Eng. J.* **2000**, *22*, 90–97.
3. He, W.; Yuan, D.; Ge, W.; Luo, H. Determination of the slip rate of the lenglongling fault in the middle and eastern segment of the Qilian mountain active fault zone. *Earthquake* **2010**, *30*, 131–137. [CrossRef]
4. Jiang, W. Holocene Rupture Pattern, Seismic Recurrence Feature of the Lenglongling Fault Zone and Its Tectonic Implication for the Northeast Tibetan Plateau. Ph.D. Thesis, Institute of Geology, China Earthquake Administration, Beijing, China, 2016.
5. Guo, P.; Han, Z.; Dong, S. Surface rupture and slip distribution along the Lenglongling fault in the NE Tibetan Plateau: Implications for faulting behavior. *J. Asian Earth Sci.* **2019**, *172*, 190–207. [CrossRef]
6. Xu, X.; Wu, X.; Yu, G.; Tan, X.; Li, K. Seismo-geological signatures for identifying M $\geq$ 7.0 earthquake risk areas and their preliminary application in mainland China. *Seismol. Geol.* **2017**, *39*, 2. (In Chinese) [CrossRef]
7. Li, Y.; Jiang, W.; Zhang, J.; Luo, Y. Space Geodetic Observations and Modeling of 2016 Mw 5.9 Menyuan Earthquake: Implications on Seismogenic Tectonic Motion. *Remote Sens.* **2016**, *8*, 519. [CrossRef]
8. Xu, Y.; Guo, X.; Feng, L. Relocation and focal mechanism solutions of the MS6.9 Menyuan earthquake sequence on January 8, 2022 in Qinghai Province. *Acta Seismol. Sin.* **2022**, *44*, 1–15. [CrossRef]
9. Guo, P.; Han, Z.; Mao, Z. Paleoearthquakes and Rupture Behavior of the Lenglongling Fault: Implications for Seismic Hazards of the Northeastern Margin of the Tibetan Plateau. *J. Geophys. Res. Solid Earth* **2019**, *124*, 1520–1543. [CrossRef]
10. Deng, Q.; Zhang, P.; Ran, Y.; Min, W.; Yang, X.; Chu, Q. Basic characteristics of active tectonics of China. *Sci. China* **2003**, *46*, 356–372.
11. Zhang, P.; Wang, Q.; Ma, Z. GPS Velocity Field and Active Crustal Blocks of Contenporary Tectonic Deformation In Continental China. *Earth Sci. Front.* **2002**, *9*, 430–441.
12. Fan, L.; Li, B.; Liao, S.; Jiang, C.; Fang, L. Precise relocation of the aftershock sequences of the 2022 M6.9 Menyuanearthquake. *Earthq. Sci.* **2022**, *35*, Q20220008. [CrossRef]
13. Liang, S.; Gan, W.; Shen, C.; Xiao, G.; Liu, J.; Chen, W. Three-dimensional velocity field of present-day crustal motion of the Tibetan Plateau derived from GPS measurements. *J. Geophys. Res. Solid Earth* **2013**, *118*, 5722–5732. [CrossRef]
14. Zheng, W.J.; Zhang, P.Z.; He, W.G.; Yuan, D.Y.; Shao, Y.X.; Zheng, D.W. Transformation of displacement between strike-slip and crustal shortening in the northern margin of the Tibetan Plateau: Evidence from decadal GPS measurements and late quaternary slip rates on faults. *Tectonophysics* **2013**, *584*, 267–280. [CrossRef]
15. Tang, J.; Zhan, Y.; Zhao, G.; Deng, Q.; Wang, J.; Chen, X.; Zhao, J.; Xuan, F. Electrical conductivity structure of the crust and upper mantle in the northeastern margin of the Qinghai_Tibet plateau along the profile Maqên-Lanzhou-Jingbian. *Chin. J. Geophys.* **2005**, *48*, 1205–1216. [CrossRef]
16. Yuan, D.Y.; Ge, W.P.; Chen, Z.W.; Li, C.Y.; Wang, Z.C.; Zhang, H.P. The growth of northeastern Tibet and its relevance to large-scale continental geodynamics: A review of recent studies. *Tectonics* **2013**, *32*, 1358–1370. [CrossRef]
17. Liu, J.; Ren, Z.K.; Zhang, H.; Li, C.; Zhang, Z.; Zheng, W. Slip rates of the Laohushan fault and the along strike-slip rate spatial pattern of the Haiyuan fault zone. *Tectonics* **2021**, *41*, e2021TC006992. [CrossRef]
18. Pan, S.; Niu, F. Large contrasts in crustal structure and composition between the Ordos plateau and the NE Tibetan plateau from receiver function analysis. *Earth Planet. Sci. Lett.* **2021**, *303*, 291–298. [CrossRef]
19. Wang, H.; Gao, R.; Zeng, L.; Kuang, Z.; Xue, A.; Li, W. Crustal structure and Moho geometry of the northeastern Tibetan Plateau as revealed by Sinoprobe-02 deep seismic-reflection profiling. *Tectonophysics* **2014**, *636*, 32–39. [CrossRef]
20. Li, Y.; Jiang, W.; Zhang, J.; Li, B.; Yan, R.; Wang, X. Sentinel-1 SAR-Based coseismic deformation monitoring service for rapid geodetic imaging of global earthquakes. *Nat. Hazards Res.* **2021**, *1*, 11–19. [CrossRef]
21. Tadono, T.; Ishida, H.; Oda, F.; Naito, S.; Minakawa, K.; Iwamoto, H. Precise Global DEM Generation By ALOS PRISM, ISPRS Annals of the Photogrammetry. *Remote Sens. Spat. Inf. Sci.* **2014**, *II-4*, 71–76.
22. Chen, C.W.; Zebker, H.A. Network approaches to two-dimensional phase unwrapping: Intractability and two new algorithms. *J. Opt. Soc. Am.* **2000**, *17*, 401–414. [CrossRef] [PubMed]
23. Yu, C.; Penna, N.T.; Li, Z. Generation of real-time mode high-resolution water vapor fields from GPS observations. *J. Geophys. Res. Atmos.* **2017**, *122*, 2008–2025. [CrossRef]
24. Yu, C.; Li, Z.; Penna, N.T. Interferometric synthetic aperture radar atmospheric correction using a GPS-based iterative tropospheric decomposition model. *Remote Sens. Environ.* **2018**, *204*, 109–121. [CrossRef]
25. Li, Y.; Tian, Y.; Yu, C.; Su, Z.; Jiang, W.; Li, Z.; Zhang, J.; Luo, Y.; Li, B. Present-day interseismic deformation characteristics of the Beng Co-Dongqiao conjugate fault system in central Tibet: Implications from InSAR observations. *Geophys. J. Int.* **2020**, *221*, 492–503. [CrossRef]
26. Li, Z.; Han, B.; Liu, Z.; Zhang, M.; Yu, C.; Chen, B.; Liu, H.; Du, J.; Zhang, S.; Zhu, W.; et al. Source Parameters and Slip Distributions of the 2016 and 2022 Menyuan, Qinghai Earthquakes Constrained by InSAR Observations. *Geomat. Inf. Sci. Wuhan Univ.* **2022**. [CrossRef]
27. Wang, T.; Shi, Q.; Nikkhoo, M.; Wei, S.; Barbot, D.; Dreger, R.; Bürgmann, M.; Motagh, M.; Chen, F. The rise, collapse, and compaction of Mt. Mantap from the September 3 2017 North Korean nuclear test. *Science* **2018**, *361*, 166–170. [CrossRef]

28. Okada, Y. Surface deformation due to shear and tensile faults in a half-space. *Bull. Seismol. Soc. Am.* **1985**, *75*, 1135–1154. [CrossRef]
29. Feng, W.; Li, Z.; Elliott, J.R.; Fukushima, Y.; Hoey, T.; Singleton, A.; Cook, R.; Xu, Z. The 2011 MW6.8 Burma earthquake: Fault constraints provided by multiple SAR techniques. *Geophys. J. Int.* **2013**, *195*, 650–660. [CrossRef]
30. King, G.; Stein, R.; Lin, J. Static stress changes and the triggering of earthquakes. *Bull. Seismol. Soc. Am.* **1994**, *84*, 935–953.
31. Shao, Z.; Xu, J.; Ma, H.; Zhang, L. Coulomb stress evolution over the past 200years and seismic hazard along the Xianshuihe fault zone of Sichuan, China. *Tectonophysics* **2016**, *670*, 48–65. [CrossRef]
32. Li, Y.; Shao, Z.; Shi, F.; Chen, L. Stress evolution on active faults in the southwestern Yunnan region, southeastern Tibetan Plateau, and implications for seismic hazard. *J. Asian Earth Sci.* **2020**, *200*, 104470. [CrossRef]
33. Wang, R.; Lorenzo-Martín, F.; Roth, F. PSGRN/PSCMP—a new code for calculating co-and post-seismic deformation, geoid and gravity changes based on the viscoelastic-gravitational dislocation theory. *Comput. Geosci.* **2006**, *32*, 527–541. [CrossRef]
34. Shao, Z.G.; Fu, R.S.; Xue, T.X.; Huang, J.P. Simulating postseismic viscoelastic deformation based on Burgers model. *J. Geod. Geodyn.* **2007**, *27*, 31–37.
35. He, J.; Lu, S.; Wang, W. Three-dimensional mechanical modeling of the GPS velocity field around the northeastern Tibetan plateau and surrounding regions. *Tectonophysics* **2013**, *584*, 257–266. [CrossRef]
36. Liu, S.; Xu, X.; Klinger, Y.; Nocquet, J.M.; Chen, G.; Yu, G.; Jónsson, S. Lower crustal heterogeneity beneath the northern Tibetan Plateau constrained by GPS measurements following the 2001 Mw7. 8 Kokoxili earthquake. *J. Geophys. Res.* **2019**, *124*, 11992–12022. [CrossRef]
37. Nalbant, S.S.; McCloskey, J.; Steacy, S.; Barka, A.A. Stress accumulation and increased seismic risk in eastern Turkey. *Earth Planet. Sci. Lett.* **2002**, *195*, 291–298. [CrossRef]
38. Xiong, X.; Shan, B.; Zheng, Y.; Wang, R. Stress transfer and its implication for earthquake hazard on the Kunlun Fault, Tibet. *Tectonophysics* **2010**, *482*, 216–225. [CrossRef]